

# Weakly nonlinear convection: Galerkin model, numerical simulation, and amplitude equation

J. Niederländer<sup>1</sup>, M. Lücke<sup>1</sup>, and M. Kamps<sup>2</sup>

<sup>1</sup> Institut für Theoretische Physik, Universität des Saarlandes, W-6600 Saarbrücken, Federal Republic of Germany

<sup>2</sup> Stabsstelle Supercomputing, Forschungszentrum Jülich, W-5170 Jülich, Federal Republic of Germany

Received July 30, 1990

The quality of three-mode Galerkin models for describing convective rolls in a fluid layer with rigid horizontal boundaries is investigated close to onset. Comparisons are made with the correct linear stability properties of the conductive state, known weakly nonlinear perturbation results for convection, and high-precision numerical solutions of the full field equations.

## I. Introduction

The three-mode Lorenz model [1] describes very well linear and weakly nonlinear convective properties close to the onset of convection in a one component fluid layer heated from below and subject to *free slip* horizontal boundary conditions: The model's marginal stability curve as a function of wave number is exact and the initial slope of the Nusselt number, i.e., of the convective heat current at onset agrees with the result of the lowest-order amplitude equation [2]. Furthermore, the lateral average of the vertical convective current through the fluid layer is independent of vertical position as is necessary to prevent local overheating.

Given this success of the free-slip Galerkin approximation [3] with analytically simple trigonometric basis functions it was natural to try also for rigid boundary conditions modes [4–7] that are analytically simple rather than the exact eigenfunctions of the linear stability problem as in the approach of Schlüter, Lortz, and Busse [8]. However, the drawbacks of this simplicity are: (i) With the above chosen [4–7] modes the linear behaviour of the model is not exact. (ii) Also the weakly nonlinear properties of the model are not exact, e.g., the initial slope of the Nusselt number at onset. (iii) The laterally averaged convective heat current varies with vertical position.

In this work we examine how well such a three-mode generalized Lorenz model which is not exact but analytically simple reproduces the linear and weakly nonlinear convective behaviour close to onset. To that end we com-

pare the linear properties with the known exact ones. For comparison of the nonlinear properties we use high precision numerical simulations of the fully nonlinear hydrodynamic field equations that we have performed and results [8, 9] of the amplitude equation for rigid boundary conditions. This equation follows from a systematic weakly nonlinear perturbation analysis close to onset. We investigate in quantitative detail the vertical as well as the lateral structure of the convective fields and their symmetry properties, the flow amplitudes, and the convective heat current as a function of Rayleigh number in a range up to twice the critical one. Note that our investigation yields also quantitative information on the range of applicability of the amplitude equation to weakly nonlinear convection.

## II. The system

We consider a fluid layer of height  $d$  between perfectly heat conducting horizontal plates extending laterally in  $x, y$  to infinity. The imposed temperature difference  $\Delta T$  between the bottom plate, at  $z = -d/2$ , and the top plate, at  $z = +d/2$ , leads to a Rayleigh number

$$R = \frac{\alpha g d^3}{\kappa \nu} \Delta T. \quad (2.1)$$

Here  $g$  is the size of the downwards gravitational acceleration,  $\kappa$  the thermal diffusivity,  $\nu$  the kinematic viscosity, and  $\alpha$  the thermal expansion coefficient.

In Oberbeck-Boussinesq approximation the equations for the deviations  $\mathbf{u} = (u, v, w)$ ,  $\theta$ ,  $p$  of velocity, temperature, and pressure from the conductive state are

$$(\partial_t + \mathbf{u} \cdot \nabla) \mathbf{u} = -\nabla p + \sigma(\theta \mathbf{e}_z + \nabla^2 \mathbf{u}) \quad (2.2a)$$

$$\nabla \cdot \mathbf{u} = 0 \quad (2.2b)$$

$$(\partial_t + \mathbf{u} \cdot \nabla) \theta = R w + \nabla^2 \theta \quad (2.2c)$$

where  $\sigma$  is the Prandtl number and  $\mathbf{e}_z$  is the unit vector in  $z$  direction. Length, time,  $\theta$ ,  $\mathbf{u}$ , and  $p$  are measured

in units of  $d$ ,  $d^2/\kappa$ ,  $\nu\kappa/(\alpha g d^3)$ ,  $\kappa/d$ , and  $\rho_0 \kappa^2/d^2$ , respectively. Here  $\rho_0$  is the constant mass density of the fluid.

We impose rigid boundary conditions at  $z = \pm 1/2$  so that there

$$w = \partial_z w = \theta = \partial_z^2 \theta = 0. \quad (2.3)$$

### A. The model

We shall describe convective flow with  $v=0$  in the form of straight rolls with axes parallel to the  $y$ -direction and wave-length  $\lambda = 2\pi/k$  as seen in experiments. To that end we express the hydrodynamic fields by a spatial mode expansion [6] in close analogy to the Lorenz model [1] for free-slip boundary conditions with basis functions appropriate to rigid boundary conditions

$$w(x, z; t) = 2\hat{u}_{101}(t) \cos(kx) C_1(\lambda_1 z) \quad (2.4a)$$

$$u(x, z; t) = -\frac{2}{k} \hat{u}_{101}(t) \sin(kx) \partial_z C_1(\lambda_1 z) \quad (2.4b)$$

$$\theta(x, z; t) = 2\sqrt{2} \hat{\theta}_{101}(t) \cos(kx) \cos(\pi z) - \sqrt{2} \hat{\theta}_{002}(t) \sin(2\pi z). \quad (2.4c)$$

Here

$$C_1(\lambda_1 z) = \frac{\cosh(\lambda_1 z)}{\cosh(\lambda_1/2)} - \frac{\cos(\lambda_1 z)}{\cos(\lambda_1/2)} \quad (2.5)$$

is the first Chandrasekhar [10] function. The eigenvalue  $\lambda_1 = 4.73$  is determined by the boundary condition  $\partial_z w = 0$  at  $z = \pm 1/2$ . In the three-mode truncation [5] of Gresho and Sani's [4] Galerkin expansion the Chandrasekhar function  $C_1$  in (2.4a, b) is replaced by  $\sqrt{8/3} \cos^2(\pi z)$ . The difference between these two functions being small also the results of the corresponding two models differ only slightly [7].

Projecting the Oberbeck-Boussinesq equations (2.2) onto the four modes of the Ansatz (2.4) with the scalar product

$$\langle fg \rangle = \frac{1}{\lambda} \int_0^\lambda dx \int_{-\frac{1}{2}}^{\frac{1}{2}} dz f^* g \quad (2.6)$$

one obtains the following system of equations

$$\tau \dot{X} = \tilde{\sigma}(Y - X) \quad (2.7a)$$

$$\tau \dot{Y} = -Y + X(r - Z) \quad (2.7b)$$

$$\tau \dot{Z} = -bZ + XY. \quad (2.7c)$$

It has the same structure as the free-slip Lorenz model, however, the parameters and the variables are slightly different. The reduced mode amplitudes are

$$X(t) = \frac{4\sqrt{2}\pi a_1}{k^2 + \pi^2} \hat{u}_{101}(t) \quad (2.8a)$$

$$Y(t) = \frac{4\pi a_3}{R_{sb}} \hat{\theta}_{101}(t) \quad (2.8b)$$

$$Z(t) = \frac{-2\pi\sqrt{2}a_3}{R_{sb}} \hat{\theta}_{002}(t). \quad (2.8c)$$

The parameters are

$$\tau = \frac{1}{k^2 + \pi^2}; \quad b = 4\pi^2 \tau; \quad \tilde{\sigma} = \frac{k^4 - 2k^2 a_4 + \lambda_1^4}{(k^2 + \pi^2)(k^2 - a_4)} \sigma \quad (2.9)$$

and

$$r = R/R_{sb}(k) \quad (2.10a)$$

is the Rayleigh number reduced by the value on the stability boundary

$$R_{sb}(k) = \frac{(k^2 + \pi^2)(k^4 - 2k^2 a_4 + \lambda_1^4)}{2k^2 a_2^2} \quad (2.10b)$$

of the model. The numbers  $a_n$  in (2.8–2.10) are given by scalar products

$$a_1 = \langle C_1 \cos(\pi z) \cos(2\pi z) \rangle = 2\pi \lambda_1^2 \left[ \frac{1}{\lambda_1^4 - \pi^4} - \frac{3}{\lambda_1^4 - 81\pi^4} \right] = 0.406 \quad (2.11a)$$

$$a_2 = \langle C_1 \cos(\pi z) \rangle = \frac{4\pi \lambda_1^2}{\lambda_1^4 - \pi^4} = 0.697 \quad (2.11b)$$

$$a_3 = a_1/a_2 = 0.582 \quad (2.11c)$$

$$a_4 = \langle C_1 \partial_z^2 C_1 \rangle = 2\lambda_1 \tanh(\lambda_1/2) - \lambda_1^2 \tanh^2(\lambda_1/2) = -12.303. \quad (2.11d)$$

### B. Numerical simulation

In our numerical simulation we have integrated the full time dependent equations for the velocity fields  $u$  and  $w$ , the pressure  $p$ , and the total temperature  $T$  all depending on  $x, z$  for a fluid with Prandtl number  $\sigma = 1$ . The integration domain in the  $x-z$  plane had length 2, i.e., the critical wave-length  $\lambda_c \simeq 2$  for rigid horizontal boundary conditions. Laterally the boundary conditions were periodic.

We used the MAC [11] method to discretize the fields on three staggered grids with uniform spacing  $\Delta x = \Delta z = 0.025$ . Spatial derivatives were replaced by central differences and time derivatives by forward differences with a time step  $\Delta t = 1.25 \times 10^{-4}$ . To determine the pressure we used a variant [12] of the SOLA code [13]. The critical Rayleigh number for onset of convection in the discretized system of equations,  $R_c = 1702$ , is about 0.34% smaller than the theoretical one,  $R_c = 1707.8$ . This we found by extrapolating the stationary squared flow amplitudes and the convective currents that were obtained for several supercritical values of  $R$ .

### III. Stability behaviour of the conductive state

Here we compare the model's stability properties of the conductive state with exact results [10, 14] that have been obtained analytically or numerically.

The eigenvalues of the system (2.7) linearized around the conductive fixed point  $X = Y = Z = 0$  are

$$\gamma_{1,2} = -\frac{\tilde{\sigma} + 1}{2} \pm \sqrt{\left[\frac{\tilde{\sigma} + 1}{2}\right]^2 + \tilde{\sigma}(r-1)}; \quad \gamma_3 = -b. \quad (3.1)$$

So the stability boundary of the conductive state is given by  $r=1$ , i.e.,  $R = R_{sb}(k)$  (2.10b). The critical values of this curve

$$R_c = 1728.4; \quad k_c = 3.098 \quad (3.2)$$

agree within 1.2% and 0.8%, respectively, with the exact results [10]  $R_c = 1707.8$ ,  $k_c = 3.117$  (the three-mode truncation [5] of Gresho and Sani [4] has  $R_c = 1824.7$ ,  $k_c = 3.101$ ). For the reduced curvature of the stability boundary at  $R_c$

$$\xi_0^2 = \frac{1}{2R_c} R_{sb}'' \quad (3.3)$$

the model gives  $\xi_0 = 0.388$  which differs by 0.8% from the result of [14]. The form of the stability curve  $R_{sb}(k)$  (2.10b) agrees also further away from the critical point very well with the exact one.

The growth rate for infinitesimal deviations from the conductive state

$$s = \gamma_1 / \tau \quad (3.4)$$

is determined by the largest eigenvalue. In order to compare with the exact results of [14] we have computed the growth rate amplitude of the model

$$s_0 = \lim_{\varepsilon \rightarrow 0} \frac{s(k_c, \varepsilon)}{\varepsilon} = \frac{100\sigma}{2.642 + 5.138\sigma} \quad (3.5)$$

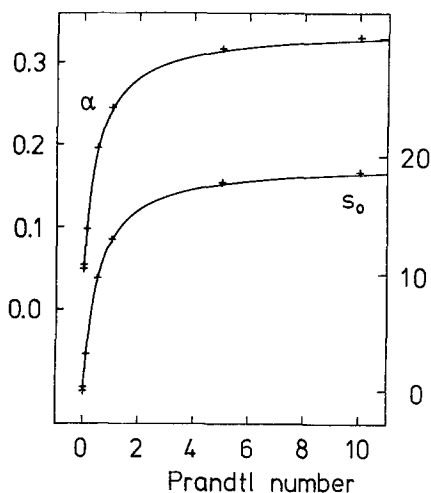


**Fig. 1.** Initial slopes  $s_0$ (3.5) and  $\alpha$ (3.6) of the growth rate and of the wave number of maximal growth, respectively, versus Prandtl number. Lines represent the model and crosses the result of [14]

and the wave number  $k_m(\varepsilon)$  of maximal growth rate, expressed in terms of

$$\alpha = \lim_{\varepsilon \rightarrow 0} \frac{k_m(\varepsilon) - k_c}{\varepsilon k_c} = \frac{1 + 13.91\sigma}{20.96 + 40.76\sigma}. \quad (3.6)$$

Here and in the following  $\varepsilon$  is defined by

$$\varepsilon = R/R_c - 1. \quad (3.7)$$

Figure 1 shows that  $s_0$  (3.4) and  $\alpha$  (3.5) agree very well with the exact results [14] over a wide range of Prandtl numbers  $\sigma$ .

### IV. Convection

In this section we compare various convective properties of stationary straight parallel rolls resulting from the model, from our numerical simulation, and from the amplitude equation [8, 9]. To that end we fix the wave number to the respective critical one for each method and use as control parameter  $\varepsilon$  (3.7) defined relative to the respective critical Rayleigh number.

Convection in the model is determined by the fixed point

$$X = Y = \pm \sqrt{b(r-1)}; \quad Z = r-1 \quad (4.1)$$

of (2.7) that is stable for  $r > 1$  and that fixes the mode amplitudes of the fields (2.4). Note that for  $k = k_c$  we have  $r-1 = \varepsilon$  in (4.1) since  $R_{sb}(k = k_c) = R_c$ .

#### A. Vertical variation of convective fields

In Fig. 2a we show as a representative example the vertical velocity  $w$  as a function of  $z$  at the lateral position of maximal upflow between two rolls -  $x=0$  in (2.4a). The profile of  $w(z)$  given in the model by the first Chandrasekhar function as well as the flow amplitude is in good agreement with the amplitude equation and with the numerical simulation for  $\varepsilon$ , say, less than 0.5. Then also upflow and downflow velocities are still of same absolute size. Note, however, that the profile  $w(z)$  obtained in our high precision simulation of the full system is at  $\varepsilon=0.1$  definitely no longer symmetric around mid height,  $z=0$ , as the profile of the model or of the amplitude equation.

In Fig. 2b we show the vertical variation of the deviation  $\theta(x, z)$  of the temperature from the conductive linear profile at the three lateral positions of maximal upflow ( $x=0$ ), roll center ( $x=\lambda/4$ ), and of maximal downflow ( $x=\lambda/2$ ).

For the sake of completeness we have also included in Fig. 2b the  $\theta$ -profiles resulting from the lowest-order amplitude equation (dashed lines), i.e., from the linear stability analysis. Being mirror symmetric around mid-height,  $z=0$ , they clearly demonstrate that the  $\sqrt{\varepsilon}$ -order result of the perturbation [8, 9] expansion is no longer adequate to describe the temperature field at  $\varepsilon=0.1$ .

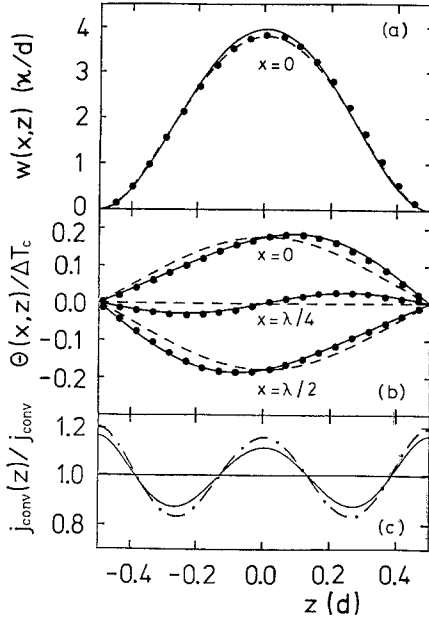


**Fig. 2a-c.** Convective fields as function of vertical position  $z$ : **a** vertical velocity,  $w$ , at  $x=0$  (lateral position of maximal upflow); **b** deviation,  $\theta$ , from the conductive temperature profile divided by the temperature difference,  $\Delta T$ , at  $x=0$ ,  $x=\lambda/4$  (center of roll), and  $x=\lambda/2$  (maximal downflow). Full lines represent the model, dashed lines the amplitude equation, and dots (every second one is shown) the numerical simulation, all for  $\varepsilon=0.104$ ,  $\sigma=1$ . **c** Vertical oscillation of the laterally averaged convective heat current of three-mode Galerkin models. Full line: our model, dash-dotted line: model of [4, 5]

### B. Flow amplitudes

For small  $\varepsilon$  the square,  $w_{\max}^2$ , of the maximal upflow velocity grows linearly with  $\varepsilon$

$$\lim_{\varepsilon \rightarrow 0} w_{\max}^2 / \varepsilon = S \quad (4.2)$$

with an initial slope  $S$ , at onset that is listed in Table 1 for the model, the simulation, and the amplitude equation. While the latter two agree very well the former is larger by 8.5%. That the model yields larger convective flow is also visible in Fig. 2a. In our simulation we found that the slope of  $w_{\max}^2$  increases with increasing  $\varepsilon$ . In the range  $\varepsilon < 1$  our numerical data are represented by the fit

$$w_{\max}^2 = 139.4\varepsilon[1 + 0.025\sqrt{\varepsilon} + 0.09\varepsilon]. \quad (4.3)$$

Note the correction  $\sim \varepsilon^{3/2}$  that is also to be expected from a perturbation analysis in powers of  $\sqrt{\varepsilon}$  of the Overbeck-Boussinesq equations.

**Table 1.** Slope,  $S$ (4.2), of  $w_{\max}^2$  and inverse slope,  $g$ (4.4), of the Nusselt number at threshold each for a Prandtl number  $\sigma=1$

	Model	Simulation	Amplitude equation [8, 9]
$S$	151.2	139.4	139.1
$g$	0.677	0.707	0.703

### C. Nusselt number and convective heat current

For small supercritical driving  $\varepsilon$  the Nusselt number grows at lowest order as

$$N = 1 + g^{-1}\varepsilon. \quad (4.4)$$

The values of  $g$  of the model [ $g=2(a_1/a_2)^2$ ], the simulation, and the amplitude equation are listed in Table 1 for a Prandtl number  $\sigma=1$ . The deviation of the model's initial slope of the Nusselt number from the simulation is 4.4% (in the three-mode truncation [5] of Gresho and Sani [4] one has  $S=150.248$  and  $g=0.72$  [15]).

Similar to  $w_{\max}^2$  also  $N$  increases stronger with  $\varepsilon$  than linearly in our simulation. In the range  $\varepsilon < 1$  our data are represented by

$$j_{\text{conv}} = 1.414\varepsilon[1 + 0.038\sqrt{\varepsilon} + 0.078\varepsilon] \quad (4.5)$$

as shown in Fig. 3 by the dotted line. Here we identify

$$j_{\text{conv}} = (N-1)R/R_c \quad (4.6a)$$

with the total spatial average

$$\langle j_{\text{conv}}(x, z) \rangle = \frac{1}{\lambda} \int_0^\lambda dx \int_{-\frac{\lambda}{2}}^{\frac{\lambda}{2}} dz [w(x, z) - \partial_z] \theta(x, z) / R_c \quad (4.6b)$$

of the vertical convective heat current reduced by the current,  $R_c$ , at threshold. The result of the lowest-order amplitude equation is shown by the dashed line and that of our model by the full line.

There are three points to note: (i) Already at  $\varepsilon=0.1$  the convective current of the full numerical solution is by 2% larger than the result  $g^{-1}\varepsilon$  of the amplitude equation. (ii) In the model  $g=0.677$  is independent of Prandtl number while in the numerical simulation and the amplitude equation [8, 9]  $g$  is  $\sigma$  dependent. The latter gives  $g=0.6995 - 0.0047/\sigma + 0.0083/\sigma^2$  which shows a marked variation only for small  $\sigma$ . (iii) The laterally averaged convective heat current,

$$j_{\text{conv}}(z) = \frac{1}{\lambda} \int_0^\lambda dx [w(x, z) - \partial_z] \theta(x, z) / R_c, \quad (4.7)$$

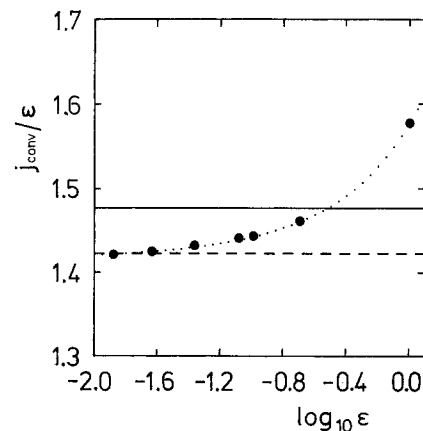


**Fig. 3.** Variation of the reduced convective current  $j_{\text{conv}}$ (4.6) with  $\varepsilon$ . Full line represents the model (2.7), dashed line the amplitude equation (4.5), dots the numerical simulation, and dotted line the fit (4.5) to the latter. Prandtl number  $\sigma=1$

is not constant in the model but oscillates as a function of  $z$  slightly around the total spatial mean,  $j_{\text{conv}}$ , c.f. the dashed curve in Fig. 2c. In particular, the model's current at the plates,  $j_{\text{conv}}(z = \pm 1/2)$ , is larger by about 16.3% than the spatial mean. Also the three-mode truncations using  $\cos^2(\pi z)$  for  $w$  show this behaviour (dash-dotted curve in Fig. 2c). This deficiency of the model – a variation of  $j_{\text{conv}}(z)$  with  $z$  would imply local heating or cooling – can be cured in a purely ad hoc manner by modifying the  $z$ -dependence of the current carrying mode  $\hat{\theta}_{002}$  in such a way as to guarantee  $j_{\text{conv}}$  (4.7) to be constant. The vertical convective heat current of the amplitude equation is independent of  $z$  and in our numerical simulation the deviation of  $j_{\text{cond}}(z)/j_{\text{conv}}$  from 1 was less than  $10^{-4}$ .

#### D. Symmetry of convective fields

Within the numerical accuracy of our simulation the convective fields  $\phi(x, z)$  showed in the driving range investigated here the following symmetry behaviour under the combined operations of lateral translation by  $\lambda/2$  and mirror imaging at the horizontal midplane

$$\phi(x + \lambda/2, -z) = \pm \phi(x, z) \quad (4.8)$$

with  $+$  for  $u, p$  and  $-$  for  $w, \theta$ . This symmetry has first been observed [16] in traveling wave convection in binary fluid mixtures where right- and left-turning rolls are not mirror images of each other. Our stationary rolls, however, do show in addition to the more general symmetry (4.8) also the mirror symmetry of left and right turning rolls:  $\phi(x, z) = \pm \phi(-x, z)$  when  $x=0$  is a position of up- or downflow with  $+$  for  $w, \theta, p$  and  $-$  for  $u$ . Combining this symmetry with (4.8) results in the previously known inversion symmetry around a roll center.

#### E. Lateral Fourier analysis

We have performed a lateral Fourier analysis of the fields obtained in our numerical simulation to compare magnitudes and  $\varepsilon$ -behaviour of their mode amplitudes with the two other methods. Theoretical results from perturbation expansions around thresholds have been presented by Busse [17] and Normand et al. [18]. They are discussed in comparison with experiments by Dubois and Bergé [19]. We discuss below the lateral Fourier modes of  $w$  and of  $\theta$  at some representative vertical positions, e.g.,  $z=0$  and  $z = \pm 0.25$ .

**1. Vertical velocity field.** The Fourier analysis of the  $x$ -dependence of the vertical component of the velocity field in the middle of the fluid layer shows that in the  $\varepsilon$  range considered in this work this field is very well represented by a few cosine modes

$$w(x, z=0) = \sum_{n=1} \hat{w}_n(z=0) \cos(nkx) \quad (k=\pi). \quad (4.9)$$

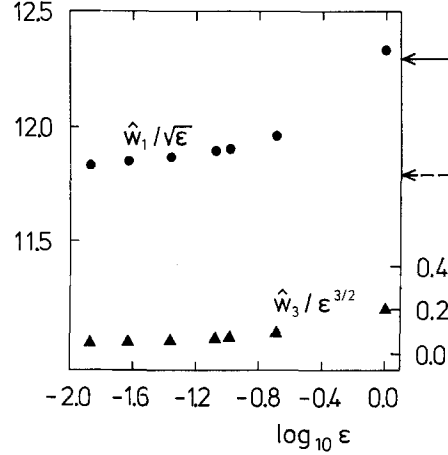


Fig. 4. Variation of the lateral Fourier amplitudes  $\hat{w}_1$  (dots), and  $\hat{w}_3$  (triangles) of the numerically obtained vertical velocity field  $w$ (4.9) at  $z=0$  with  $\varepsilon$  for  $\sigma=1$ . Here  $w$  is measured in units of  $\kappa/d$ . Solid arrow represents the model ( $\hat{w}_1 = 12.296\sqrt{\varepsilon}$ ) and dashed arrow the amplitude equation ( $\hat{w}_1 = 11.794\sqrt{\varepsilon}$ )

The amplitudes of the sine modes vanish due to the mirror symmetry of left and right turning convection rolls. Also the cosine modes with even  $n$  are zero within our numerical resolution in accordance with the symmetry (4.8) which translates into  $\hat{w}_n(z) = (-1)^{n+1} \hat{w}_n(-z)$ .

The analysis shows that even for  $\varepsilon \approx 1$   $\hat{w}_1$  is still about 6 times larger than the next relevant mode amplitude  $\hat{w}_3$  and for small  $\varepsilon$  the ratio  $\hat{w}_3/\hat{w}_1 \approx 0.004\sqrt{\varepsilon}$ . So  $w(x, z=0)$  is reasonably well approximated by using only the predominant mode  $\hat{w}_1$ . The  $\varepsilon$  dependence of  $\hat{w}_1$  is shown in Fig. 4. Only in the limit of small  $\varepsilon$  it is given by

$$\hat{w}_1 = 11.8\sqrt{\varepsilon}. \quad (4.10)$$

The model ( $\hat{w}_1 = 12.296\sqrt{\varepsilon}$ ) as well as the amplitude equation ( $\hat{w}_1 = 11.794\sqrt{\varepsilon}$ ) show the  $\sqrt{\varepsilon}$ -variation for all  $\varepsilon$  as indicated in Fig. 4 by the solid and dashed arrows, respectively. From experiments done at larger  $\varepsilon$  Dubois and Bergé [19] inferred a growth behaviour of the first mode  $\hat{w}_1 = (12.6 \pm 0.4) \varepsilon^{0.5 \pm 0.02}$  without further corrections.

In our simulation the next important mode is  $\hat{w}_3 \cos(3kx)$ . Its  $\varepsilon$  dependence is shown in Fig. 4 as well. In the limit of small  $\varepsilon$  we found that  $\hat{w}_3$  is given by

$$\hat{w}_3 = 0.046 \varepsilon^{3/2}. \quad (4.11)$$

Also this mode shows additional growth with increasing  $\varepsilon$ . The large  $\varepsilon$  experimental results of Dubois and Bergé [19] for  $\hat{w}_3$  were parametrized by  $\hat{w}_3 = (0.35 \pm 0.035) \varepsilon^{1.5 \pm 0.06}$ .

A Fourier analysis of  $w$  at positions  $z = \pm 0.25$  showed that also there  $\hat{w}_1$  dominates: even for  $\varepsilon=1$   $\hat{w}_1$  is about 15 times larger than  $\hat{w}_2$  and about 70 times larger than  $\hat{w}_3$ . Again the amplitudes were in accordance with the symmetry (4.8), i.e.  $\hat{w}_n(z=0.25) = (-1)^{n+1} \hat{w}_n(z=-0.25)$ . The nonvanishing of modes with even  $n$  reflects the asymmetry around midheight,  $w(x, z) \neq w(x, -z)$  (cf. Sect. IV A. and Fig. 2a).

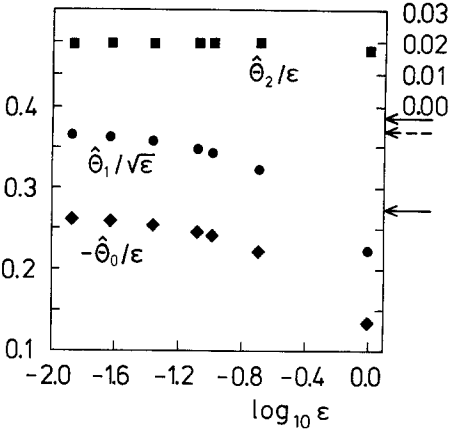


**Fig. 5.** Variation of the lateral Fourier amplitudes  $\hat{\theta}_0$  (rhombs),  $\hat{\theta}_1$  (dots), and  $\hat{\theta}_2$  (squares) of the numerically obtained reduced deviation  $\theta/\Delta T_c$  (4.12) from the conductive temperature profile at  $z = -0.25$  with  $\varepsilon$  for  $\sigma = 1$ . Solid arrows represent the model ( $\hat{\theta}_0 = -0.274\varepsilon$ ,  $\hat{\theta}_1 = 0.387\sqrt{\varepsilon}$ ) and dashed arrow the amplitude equation ( $\hat{\theta}_1 = 0.371\sqrt{\varepsilon}$ )

2. *Temperature field.* Similar to the velocity field, the Fourier analysis of the  $x$ -dependence of the deviations from the conductive temperature profile at  $z = \pm 0.25$  shows that these deviations are very well represented by just a few Fourier modes

$$\frac{\theta(x, z = \pm 0.25)}{\Delta T_c} = \sum_{n=0} \hat{\theta}_n(z = \pm 0.25) \cos(nkx). \quad (4.12)$$

The only difference is that  $n$  starts with the value zero, due to  $x$ -independent deviations from the conductive profile. Again the sine modes are absent reflecting the mirror symmetry. Furthermore we checked that  $\hat{\theta}_n(z) = (-1)^{n+1} \hat{\theta}_n(-z)$  holds according to the symmetry (4.8).

The  $\varepsilon$  dependence of the first modes  $\hat{\theta}_n(z = -0.25)$  is shown in Fig. 5. For small  $\varepsilon$   $\hat{\theta}_0$  varies linearly with  $\varepsilon$

$$\hat{\theta}_0 = -0.265\varepsilon. \quad (4.13)$$

The next relevant modes are  $\hat{\theta}_1$  which is proportional to  $\sqrt{\varepsilon}$  for small  $\varepsilon$

$$\hat{\theta}_1 = 0.368\sqrt{\varepsilon} \quad (4.14)$$

and  $\hat{\theta}_2$  which is linear with  $\varepsilon$  for small  $\varepsilon$

$$\hat{\theta}_2 = 0.0194\varepsilon. \quad (4.15)$$

Note that  $\varepsilon = 1$  the first mode that is not included in the model,  $\hat{\theta}_2$ , carries the relative weight  $\hat{\theta}_2/\hat{\theta}_0 \approx -0.1$  and  $\hat{\theta}_2/\hat{\theta}_1 \approx 0.08$  as can be read off from Fig. 5. Higher modes are less important, e.g.,  $\hat{\theta}_3/\hat{\theta}_2 \approx 0.4$  at  $\varepsilon = 1$ .

## V. Summary and Discussion

The critical Rayleigh number and the critical wave number of our three mode Galerkin model agree within 1.2% and 0.8%, respectively, with the exact results. Also

the stability curve near the critical point, the growth rate, and the wave number for maximal growth rate agree very well.

The nonlinear convective properties of the model, however, show larger deviations from our high precision numerical solution of the full field equations. While the shape of the profile  $w(z)$  of the model's vertical velocity agrees quite well with that of the simulation the squared convective flow amplitudes of the former are for  $\sigma = 1$  close to threshold by about 8.5% larger than the latter. The model's convective flow intensity and convective current grow linear in  $\varepsilon$  as does the lowest order amplitude equation while the numerical solution shows steeper growth for both (at  $\varepsilon = 0.1$  the deviation from the linear behaviour of  $j_{\text{conv}}$  is already 2%). A more serious limitation of the model's applicability is the fact that the model's initial slope of the Nusselt number is independent of Prandtl number while the correct slope shows for  $\sigma \ll 1$  a strong variation with  $\sigma$ .

A lateral Fourier analysis of the numerically obtained convective fields at different vertical positions shows that the three modes of the truncation (2.4) are the dominant ones in the range  $\varepsilon \leq 1$  considered in this work. However, while the latter vary as  $\sqrt{\varepsilon}$  or  $\varepsilon$  the corresponding lateral Fourier amplitudes of the simulation show clear deviations from this  $\varepsilon \rightarrow 0$  asymptotic behaviour.

The vertical convective temperature profiles taken, e.g., at the lateral positions of maximal upflow, downflow, and roll center show already at  $\varepsilon = 0.1$  large deviations from the vertical mirror symmetry at midplane that one obtains to lowest order,  $\sqrt{\varepsilon}$ , in a perturbation expansion [8, 9]. The model's temperature profiles do reflect via the additional mode  $\sim \sin(2\pi z)$  this asymmetry. Small differences to the numerical profiles are the reason that the laterally averaged convective heat current  $j_{\text{conv}}$  instead of being  $z$ -independent shows variations around its mean of relative size up to 16%. A simple, ad hoc way to eliminate this deficiency would be to change the  $z$ -dependence of the contribution  $\sim \theta_{002} \sin(2\pi z)$  to the temperature field such as to guarantee a constant  $j_{\text{conv}}$ . But even so the initial slope of the Nusselt number (flow intensity) at onset would be still too large by 3% (7%).

All in all the model describes for not too small Prandtl number fluids the convective roll fields rather well. Even at twice the critical Rayleigh number,  $\varepsilon = 1$ , the ratios of the magnitudes of the next important lateral Fourier modes,  $\hat{w}_2, \hat{w}_3, \hat{\theta}_2$ , that were discarded in the model to the dominant incorporated ones are only  $\hat{w}_2/\hat{w}_1 \approx 0.07$ ,  $\hat{w}_3/\hat{w}_1 \approx 0.17$ , and  $\hat{\theta}_2/\hat{\theta}_0 \approx 0.1$ .

Finally we mention that the convective fields obtained in the numerical simulation show in addition to the symmetry of left- and right-turning rolls also a newly discovered symmetry behaviour under lateral translation by half a wavelength combined with vertical mirror imaging at midheight of the fluid layer.

This work was supported by the Volkswagen-Stiftung.

## References

1. Lorenz, E.N.: J. Atmos. Sci. **20**, 130 (1963)
2. Newell, A.C., Whitehead, J.A.: J. Fluid Mech. **38**, 279 (1969)
3. Finlayson, B.A.: The method of weighted residuals and variational principles. New York: Academic Press 1972
4. Gresho, P.M., Sani, R.L.: J. Fluid Mech. **40**, 783 (1970)
5. Ahlers, G., Hohenberg, P.C., Lücke, M.: Phys. Rev. A **32**, 3493 (1985); *ibid.* 3519 (1985)
6. Edwards, B.F., Fetter, A.L.: Phys. Fluids **27**, 2795 (1984)
7. Niederländer, J.: Diploma thesis. Saarbrücken, 1986 (unpublished)
8. Schlüter, A., Lortz, D., Busse, F.: J. Fluid Mech. **23**, 129 (1965)
9. Cross, M.C.: Phys. Fluids **23**, 1727 (1980)
10. Chandrasekhar, S.: In: Hydrodynamic and hydromagnetic stability. New York: Dover 1981
11. Welch, J.E., Harlow, F.H., Shannon, J.P., Daly, B.J.: Los Alamos Scientific Laboratory Report No. LA-3425, 1966
12. Lücke, M., Mihelcic, M., Kowalski, B., Wingerath, K.: In: The physics of structure formation: Theory and simulation. Güttinger, W., Dangelmayr, G. (eds.), p. 97. Berlin, Heidelberg, New York: Springer 1987
13. Hirt, C.W., Nichols, B.D., Romero, N.C.: Los Alamos Scientific Laboratory Report No. LA-5652, 1975
14. Dominguez-Lerma, M.A., Ahlers, G., Cannell, D.S.: Phys. Fluids **27**, 856 (1984)
15. In Ref. 5 the *laterally* averaged convective heat current was evaluated at the lower plate
16. Barten, W., Lücke, M., Hort, W., Kamps, M.: Phys. Rev. Lett. **63**, 376 (1989)
17. Busse, F.H.: J. Math. Phys. **46**, 140 (1967)
18. Normand, C., Pomeau, Y., Velarde, M.G.: Rev. Mod. Phys. **49**, 581 (1977)
19. Dubois, M., Bergé, P.: J. Fluid Mech. **85**, 641 (1978)